doi:10.26443/seismica.v5i1.1175

SEISMICA

Imaging the North Bishop Block with Ambient Noise and Converted Phases Observed through Fiber-Optic Seismology

Eli Bird [*1], **James Atterholt** [1], **Ettore Biondi** [1], **Yan Yang** [1], **Zhongwen Zhan** [1]

[1]Seismological Laboratory, California Institute of Technology, Pasadena, USA

Author contributions: *Conceptualization*: Eli Bird, Zhongwen Zhan. *Methodology*: Eli Bird, James Atterholt, Ettore Biondi, Yan Yang, Zhongwen Zhan. *Software*: Eli Bird, James Atterholt, Yan Yang. *Formal Analysis*: Eli Bird. *Writing - Original draft*: Eli Bird. *Writing - Review & Editing*: Eli Bird, James Atterholt, Ettore Biondi, Yan Yang, Zhongwen Zhan. *Supervision*: Zhongwen Zhan.

Abstract Located in eastern California, Owens Valley is a rift basin in the western Basin and Range Province, bounded by the Sierra Nevada and White Mountains. While the basin has been the site of extensive geologic study, most interpretations of the subsurface structure depend on non-unique interpretation of gravity data. Under these constraints, past researchers have inferred the presence of the North Bishop Block, a block slumped from the White Mountains, roughly 100 square kilometers in area. A section of optical fiber near the town of Bishop, CA, in Owens Valley has been converted to a seismic array, and records apparent *Ps* converted phases above the proposed location of the North Bishop Block. We assume that the *Ps* phase is produced by the slumped block and jointly invert for a velocity structure through ambient noise cross-correlation and from the observed *Ps* phases, advancing the use of converted phases in fiber-optic seismic data. We replicate the proposed depth of the North Bishop Block and observe a deeper phase-converting interface to the south. We interpret this interface as an unmapped slumped block, located at roughly 1 kilometer depth. This result has important implications for the tectonic history and subsurface hydrology of Bishop, CA.

Production Editor:
Yen Joe Tan
Handling Editor:
Suzan van der Lee
Joseph Byrnes
Copy & Layout Editor:
Hannah F. Mark

Received:
February 26, 2024
Accepted:
June 4, 2026
Published:
June 16, 2026

1 Introduction

Owens Valley is among the westernmost rift basins forming the extensional Basin and Range province (Stevens et al., 2013). The valley strikes approximately NNW, and is bounded by the Sierra Nevada Mountains and White Mountains to its west and east, respectively (Stevens et al., 2013). Long Valley Caldera, a large volcanic crater which formed 767 kya in a rhyolitic supereruption, is located to the northeast of Owens Valley (Stevens et al., 2013; Biondi et al., 2023). Owens Valley is a critical water resource to Los Angeles County, with about 35% of the county's water transported from the valley and other sections of the Eastern Sierra by way of the Los Angeles Aqueduct (LAWDP, 2024; Danskin, 1998). Careful consideration of the subsurface geology of Owens Valley is of great scientific and societal interest, given the tectonic and volcanic activity in its vicinity and its importance as a water resource. Subsurface mapping is a critical tool in characterizing groundwater storage, constraining past eruptions from nearby volcanic systems, and informing faulting history, for example. However, while the valley has been extensively studied, major subsurface features are still poorly understood. This is exemplified by the North Bishop Block (NBB), an inferred block of material slumped off of the White Mountains, northeast of Bishop, CA (Figure 1).

In the mid-twentieth century, the United States Geological Survey (USGS) performed a gravity survey of Owens Valley and several surrounding basins, augmented by sparser additional geophysical observations, including aeromagnetic and active-source seismic experiments (Pakiser and Kane, 1962). Gravity data to the north of Bishop indicate a high-density anomaly, elevated vertically above the bedrock (Bateman et al., 1965). Decades later, the anomaly was interpreted as the slumped NBB, detached from the White Mountains to its east, with resistivity data indicating the upper surface of the block was approximately 400 meters below ground level (Hollett et al., 1989). The NBB is among the most prominent features in Owens Valley, covering roughly 100 square kilometers, but the gravity data constraining the block have inherently limited depth sensitivity (Stevens et al., 2013). Producing a feature of this size would clearly require broad-scale forces along a span of the mountains, potentially of great interest to the area's geologic history, but the exact way that extensional forces in the basin and range province would translate to slumping of material onto existing valley fill remains unclear. We take a passive seismic approach in providing a high spatial resolution picture of the block.

This study employs fiber-optic seismology, a relatively young branch of seismological instrumentation, in which an optical fiber is converted to an array of strainmeters (Zhan, 2020). Fiber-optic seismology is increasingly popular, given its ability to provide dense instrumental coverage at relatively low cost. The tech-

*Corresponding author: elijahjosephbird@gmail.com

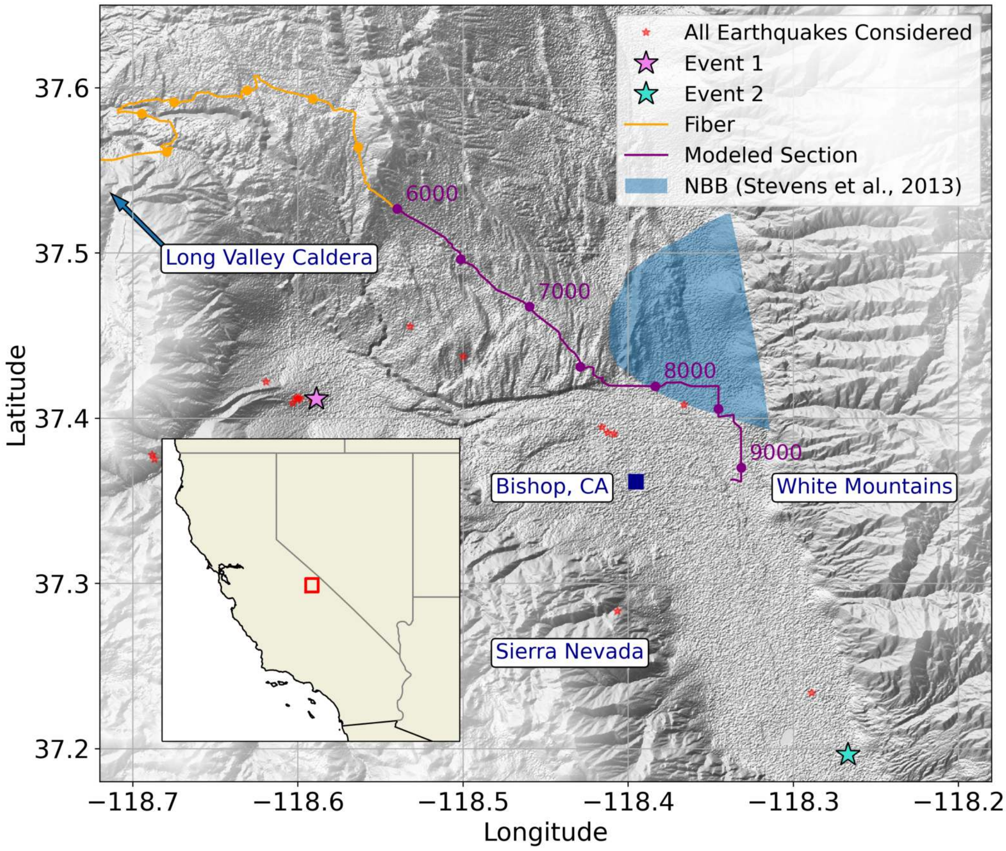

Figure 1 Map of northern Owens valley, denoting fiber channels and earthquakes considered in study. The earthquakes plotted in Figure 2 are plotted as a large turquoise and violet stars, with other earthquakes considered in the study plotted as small red stars. Orange and purple circles along the fiber denote every five-hundredth channel.

nology has been utilized in wide-ranging contexts, with applications in the study of seismicity (Yin et al., 2023; Li et al., 2023), volcanic structures (Biondi et al., 2023; Klaasen et al., 2023; Bird et al., 2025), human activity (Wang et al., 2020), weather events (Roth et al., 2023; Shen and Zhu, 2023), and ocean processes (Williams et al., 2019). One promising application of fiber-optic seismology is subsurface imaging. Partially because the scale of resolvable features is heavily tied to station density, fiber-optic seismic arrays have proven powerful in tomographic work (Dou et al., 2017; Song et al., 2022; Yang et al., 2022; Biondi et al., 2023).

Despite its advantages, fiber-optic seismology only constrains along-fiber strain (i.e., changes in the length of a span of fiber over time, which will appear in response to both *P* and *S* arrivals from an arbitrary source location. Note that as the reference frame is the initial length of the fiber, both a shearing of the fiber and a compression or extension can produce a strain, which cannot necessarily be distinguished). This makes many common methods of seismic data processing difficult to employ, including receiver functions, a typical approach in sensing delays between *P* and *Ps* phases on a seismogram to image structural discontinuities (Langston, 1979; Leahy et al., 2012). Past studies of *Ps* phases on fiber-optic seismic arrays have relied on deconvolution of direct arrivals at co-located conventional sensors to produce receiver functions (Yu et al., 2019). However, even in the absence of conventional seismic data, arrivals of converted phases on fiber-optic sensors can provide critical constraints on the depth and seismic velocity of associated earth structures with fine-scale spatial resolution (Atterholt and Zhan, 2024).

2 Data & Methods

2.1 Array Information

We use a 100 km fiber-optic array which extends from Mammoth Lakes, CA, to Bishop, CA, and crosses into Owens Valley in its final 20-30 km (Figure 1). The array records data with a channel spacing of 10 m, gauge-length of 100 m, and sampling rate of 100 Hz. Note that gauge-length is the spatial interval which is utilized in producing estimates of strain and may be treated as a moving spatial window over which strain is averaged before being output at denser channel spacing. Earthquakes recorded on the fiber where it crosses the previously proposed location of the North Bishop Block, present a coherent phase following the direct *P* arrival

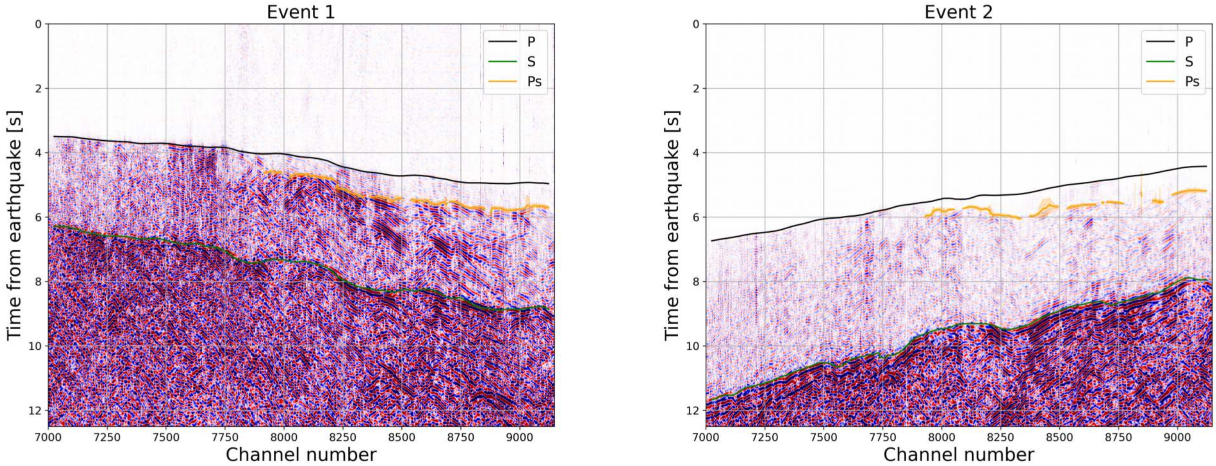

Figure 2 Example along-fiber strain rate time series for Events 1 & 2 with an interpreted *Ps* phase following *P* by less than a second for fiber channels >7900. The *P* arrival is indicated by a black line and the *Ps* arrival is indicated by an orange line. Gaps in *Ps* arrival are present where the time series does not meet the STA/LTA threshold.

(Figure 2). We assume the arrival is a converted *Ps* phase rather than a *P* multiple, as it is higher in amplitude than the direct *P* arrival. One would generally expect *P* multiples to take on a lower amplitude than direct *P* arrivals, as they should arrive at similar incidence and with increased attenuation. In contrast, converted *S* arrivals may take on higher amplitudes than *P* arrivals, especially when approaching the array at steep incidence angles. Incidence angles for *P* and *S* arrivals are plotted in Figure S1.

2.2 Ambient Noise Data

Given a velocity structure, the delay between the *P* and *Ps* phases constrains the depth of the converting structure. However, this initial velocity structure must be produced through additional data. To determine a velocity structure, we generate ambient noise shot gathers. In producing these shot gathers, we consider one week of continuous data, beginning on May 1, 2022. We use data from channels 5999 to 9147 (labelled in purple on Figure 1) at two channel intervals. We band-pass the data between 0.05 Hz and 10 Hz, decimate them to a 25 Hz sampling rate, and spectrally-whiten the signals between 0.05 Hz and 10 Hz. We then produce cross-correlations between all channel pairs. The cross-correlation of any single channel with all other channels allows it to act as a virtual source.

Rayleigh waves typically dominate cross-correlations on locally straight fibers (Fang et al., 2022). Thus, for each fiber channel, r_i, we can take a beamforming approach to determine a local Rayleigh wave phase velocity dispersion curve, as in Yang et al. (2022). We consider a sub-array of channels surrounding a central channel, r_i, and slant-stack a shot gather with source at channel s_j, which has been bandpassed at frequency f_k. In observing how waveforms from each of the virtual sources traverse the sub-array, we may approximate v_{ijk}, the phase velocity at r_i for Rayleigh waves of frequency f_k, using a virtual source at s_j.

We consider central channels, r_i, at distances of 1.5 to 3 wavelengths from the source channel, s_j, choosing to ignore signals at greater distances due to signal attenuation and those at shorter distances as our shot gathers sometimes present spurious signals close to zero lag. In slant-stacking, we would like a sufficiently long sub-array to allow for a stable measurement, but a sufficiently short sub-array to provide a reasonably local constraint on the velocity at r_i. Thus, we choose sub-array stations as those within 0.5 wavelengths of r_i, as the sub-array length required for stability should roughly scale with the wavelength. In both the constraint on sub-array width and that on source-receiver distance, we approximate the wavelength using a velocity of 2 km/s (dividing 2 km/s by the frequency in Hz).

The mean, μ_v, and variance, σ_v^2, of the frequency-dependent phase velocities that define the dispersion curves can then be defined as:

$$\mu_v^{ik} = \frac{1}{n}\sum_{j=1}^{n}(v_{ijk}) \tag{1}$$

$$(\sigma_v^{ik})^2 = \frac{1}{n}\sum_{j=1}^{n}(v_{ijk} - \mu_v^{ik})^2 \tag{2}$$

where n is the number of source channels for receiver r_i at frequency f_k. An example dispersion curve is plotted in Figure S2 and all picked dispersion curves on the array are plotted in Figure 3.

2.3 Converted Phase Data

We pick earthquake *P* arrivals using PhaseNet-DAS, an ML-based picking algorithm, trained on fiber-optic seismic data (Zhu et al., 2023). As PhaseNet-DAS is not trained to pick secondary phases, we instead pick *Ps* arrival times through short-term average/long-term average processing (STA/LTA). This choice is reasonable, as the observed *Ps* phases along the fiber are typically much higher in amplitude than the *P* phases. We apply STA/LTA to data bandpassed from 1-8 Hz, using 0.12 s short term windows and 0.3 s long term windows (see Figure S3). We spatially average the STA/LTA on a lengthscale of 500 m (50 channels) before picking arrivals. This smoothing allows for more robust arrival time picks (reduced smoothing leads to more false picks), and should not significantly impact on our final model, as we smooth our data on a similar spatial scale prior to inversion. We consider threshold STA/LTA ratios ranging from 2 to 4 at intervals of 0.1 and choose the mean phase pick across the thresholds for the lth event, t_{il} (with example phase picks shown in Figure 2). In considering the delay between *P* and *Ps* at a given channel for all events with sufficiently high-quality data, we can estimate the mean delay, μ_t^i, and the standard deviation of delay times, σ_t^i, for a single channel, (plotted in Figure 3). Considering events collectively, rather than individually, is reasonable, as the observed delay between *P* and *Ps* is large relative to its uncertainty, despite variable backazimuths across differing events.

The amplitude ratio between the *P* and *Ps* phases can provide an additional constraint on the velocity within the converting structure, with the details of this constraint discussed in more detail in subsection 2.5.2. For the ith channel, we pick the amplitude of each phase, A_i, as the maximum of the envelope in the 0.05 s preceding and 0.2 s following the picked arrival, after 500 meter spatial averaging. As with STA/LTA, this processing is performed on data bandpassed between 1 and 8 Hz. Taking the mean and standard deviation of all amplitude ratio observations, we produce a global estimate of the amplitude ratio between the P and Ps phases, μ_A with uncertainty σ_A.

Earthquakes considered in producing estimates of amplitude ratios and delay times are listed in Table S1. Due to uncertainty in coupling of ground motion to the fiber, absolute amplitude information is unreliable on fiber-optic arrays, but in considering relative amplitudes, we may ignore the effect of coupling.

2.4 Model Parameterization

We approach the tomography problem from an inference-based perspective. The philosophy of inference mode tomography encourages building existing knowledge of subsurface structure into model parameterization, providing researchers an image of the subsurface that would not necessarily be accessible through a discovery driven approach (Tsai, 2023). For our problem, we assume that a slumped block of bedrock material is in fact producing the converted phase and invert for the velocity structure at channels along the array. We assume that the first recorded *Ps* phase converts from the top of the slumped block, rather than the bottom. The top surface will produce an earlier arrival and is expected to have a higher impedance contrast, as both the overlying and underlying material likely consists of valley fill and the latter should be more compressed. Note that based on the interpretation presented here, a converted phase from lower bound of the block is also likely recorded, but will closely follow the *Ps* arrival from the top of the block, and thus be difficult to distinguish from its coda. If we were to assume that the phase was produced at the base of the block, the inverted feature would be located at slightly shallower depths.

At channels where no converted phase is observed, we invert for a four-layer *S* velocity structure solely on the basis of Rayleigh wave dispersion curves. Rayleigh wave dispersion curves have a dependence on *P* velocity and density, in addition to *S* velocity. To reduce model complexity, we assume an empirical, polynomial relationship between the quantities, as derived by Brocher (2005). We choose a four-layer model, as it represents the simplest layered model which can reasonably fit our data within error.

At channels where a converted phase is present, we additionally impose the presence of a slumped block. We make no assumptions regarding the location of the block relative to other model layers, instead parameterizing the feature in terms of its location below the ground surface. That is to say, we set the depths and thicknesses of the other four model layers and the slumped block is imposed on top of the four-layer model, replacing a portion of the model. Thus, depending on the thickness and depth of the block, it may lie between two of the other layers or within a single layer, resulting in a model with up to six layers. This approach allows for a consistent definition of the four non-block layers, both in the presence and absence of a block.

For the ith channel, assuming a converted phase is present, we invert for the velocity structure on the basis of dispersion curves, the observed delays between *P* and *Ps* phases from local earthquakes, and the ratio of amplitudes between said phases, with all data considered in a single log-likelihood function:

$$L_i = -\frac{1}{2}\left(\frac{(G(m_i)_A - \mu_A)^2}{(\sigma_A)^2} + \frac{(G(m_i)_t - \mu_t^i)^2}{(\sigma_t^i)^2} + \sum_{k=1}^{m}\frac{(G(m_i)_v^k - \mu_v^{ik})^2}{(\sigma_v^{ik})^2}\right) \quad (3)$$

Here we define $G(m_i)_A$, $G(m_i)_t$, and $G(m_i)_v$ as the predicted amplitude ratio, travel time, and dispersion curve data, respectively, for a given velocity model, m_i.

2.5 Forward Modeling of Data

Our inversion requires forward modeling of synthetic datasets from potential velocity models. Particularly, we must forward model dispersion curves and converted phases (timing and amplitude relative to the direct arrival) from arbitrary velocity models in our model space. Dispersion curves are forward modeled with the surf96 routine from Herrmann (2013), and modelling of converted phases is described in more depth, below.

2.5.1 *Ps* Timing

At any given channel, we forward model the delay between the *P* and *Ps* arrivals. We assume that the arriving energy has propagated as a plane wave across a locally

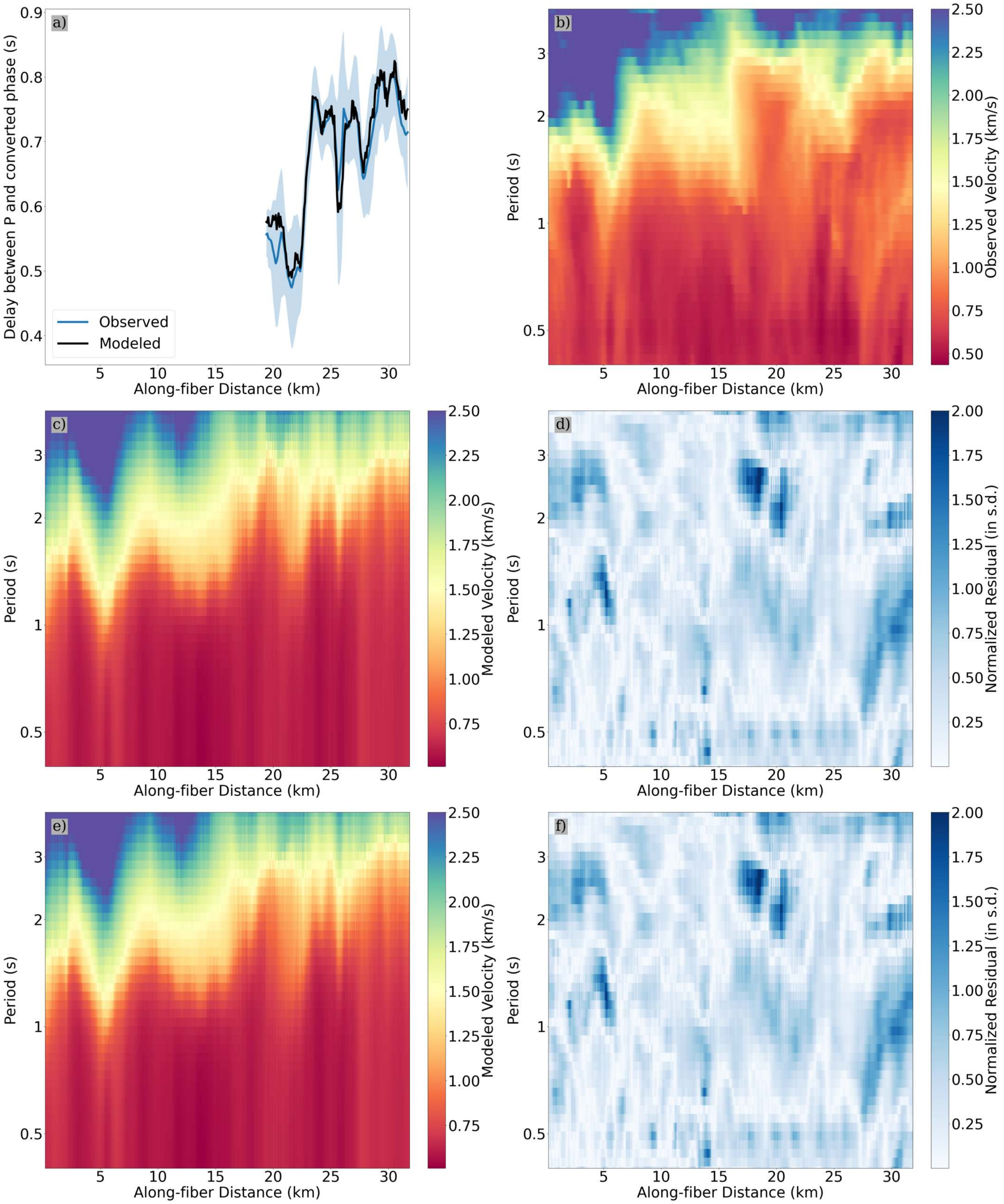

Figure 3 Fit of model to data. a) Modeled and observed time delay of *Ps* phase from direct *P* arrival with observation uncertainty plotted in light blue, b) observed Rayleigh phase velocity dispersion curves, c) modeled dispersion curves, and d) dispersion curve residuals (normalized by observation uncertainty). We also plot e) modeled dispersion curves, and f) dispersion curve residuals for an inversion using an infinitesimally thin converting layer.

horizontal, homogeneous medium. If direct and converted phases traverse a given layer with seismic velocities α and β, the contribution of the layer to the delay between the phases may be approximated as:

$$t = \frac{h\cos(\arcsin(p\beta))}{\beta} - \frac{h\cos(\arcsin(p\alpha))}{\alpha} \quad (4)$$

where p is the ray parameter and h is the layer thickness. α and β represent the *P*- and *S*-wave velocities in the layer, respectively. This equation is then the difference of the vertical slownesses for *P*- and *S*-waves multiplied by the layer height.

We roughly approximate the ray parameter between a given event/channel pair as the delay between the source time and arrival time, divided by the lateral distance of the source from the receiver. We find that the approximate ray parameters are relatively consistent across all event/channel pairs, typically ranging from 0.19 to 0.25 s/km. Thus, for each channel, we calculate a mean ray parameter across all events, used in forward modeling the *Ps*-*P* delay. Note that this approximation of the delay time assumes that both arrivals follow the same ray path at depth and remain parallel until they reach the converting boundary. This should be approximately true, as our results show that the ray parameters of the events are roughly equal to the velocity of the deepest layer in our model. This means that both rays should travel nearly horizontally through said layer. The geometry of these ray paths is clarified in Figure S4.

2.5.2 *Ps* Relative Amplitude

One can forward model the amplitude ratio between the *P* and *Ps* phases solely on the basis of seismic velocities, densities, and the ray parameter, assuming that the differing attenuation of *P* and *S* phases has minimal effect on the ratio. One may forward model the predicted particle motion on the basis of transmission coefficients for the converted and direct arrivals at the converting boundary and overlying layer boundaries (Aki and Richards, 2002). In predicting DAS amplitudes, one must also account for the polarity of *P* and *SV* particle motion relative to the direction of a span of fiber. To account for this effect, we forward model the expected particle motion associated with a given phase and project it in the direction of the fiber. Channel-by-channel measurements of the amplitude ratio appear noisy, so we fit a global estimate of this ratio and its uncertainty (Figure S5). Note that although we are measuring strain rate, our invocation of particle motion is valid, as we observe that both arrivals have a similar period (such that amplitude ratios will be preserved when taking the derivative in time).

2.6 Inversion Workflow

We perform our inversion in two steps, starting with a sparse, preliminary inversion and using it to inform a second, denser inversion. Both inversions are performed in a Markov chain Monte Carlo (MCMC) framework, implemented with the Python package emcee (Foreman-Mackey et al., 2012). At each iteration of the inversion, the algorithm proposes a step to a new location in the model space. The log-likelihood function defined by equation 3 is used to determine the relative probability of the current and proposed locations, defining an acceptance ratio in moving to the proposed location.

In our first, sparser step, we invert for one-dimensional velocity models at 500 meter steps along the length of the fiber. We apply a 2-kilometer moving average to the dispersion curve, delay time, and relative amplitude data in this run. Running the MCMC inversion on data from a given channel, we produce a model posterior distribution local to said channel. Summing the posterior distributions across all spatial steps, we can approximate a global probability distribution across the extent of the fiber. This global probability distribution is the only result from the sparse inversion which is carried over into our second step. We expect a degree of lateral continuity in earth structure, and we would like to ensure that any deviations from a homogeneous structure are required by our data. To this end, the global probability distribution for layer velocities (as calculated in the sparser inversion) is taken as a model prior in our second step. This choice means that in an instance where two velocity models are equally preferable at a location along the fiber, the denser inversion will select the velocity model whose layer velocities are more typical of global values. In the absence of the global distribution, sections of the fiber with poorly constrained dispersion data would become unstable, as a wide variety of models could fit the data within error.

We perform our second, denser inversion for one-dimensional velocity models, now considering 80-meter steps and spatially averaging data at 500-meter windows. The only change in the inversion between the sparse and dense steps is the addition of the global layer velocity probability distribution as a model prior in each of our one-dimensional inversions.

The thickness of the slumped block is only constrained by dispersion curves. As this is a relatively weak constraint, we impose a constant block thickness across all channels which observe a converted phase and determine the constant through its ability to maximize the overall model likelihood. We repeat our MCMC-based inversion with slumped blocks of thicknesses 0 m, 25 m, 50 m, 100 m, 200 m, 400 m, and 800 m, and compare the models' abilities to fit our data. This process acts as a grid search for the global block parameterization that maximizes model likelihood.

3 Results

We find that model likelihood is roughly equal for all thicknesses less than or equal to 200 meters (See Figure S6). Because we observe a clear converted phase, we represent the block as having 200 meter thickness to ensure that its thickness is at least on the same order as the wavelengths used in the study (approximately 500 meters, given the model P-velocity at the depth of the block ($\approx$ 2.7 km/s) and dominant period of the events ($\approx$ 5 Hz)). However, the thickness is not well-constrained by the inverted data, especially relative to the depth to the converting interface and the amplitude of the velocity contrast. The output velocity model and its uncertainties are displayed in Figure 4. The block takes on a velocity of 2390 m/s with a standard deviation of 40 m/s. In order of increasing depth, the remaining model layers take on mean velocities of 640, 1290, 2310, and 3350 m/s, with respective standard deviations of 40, 140, 150, and 150 m/s. Uncertainties in layer thicknesses are plotted in Figure S9. The model generally shows an excellent

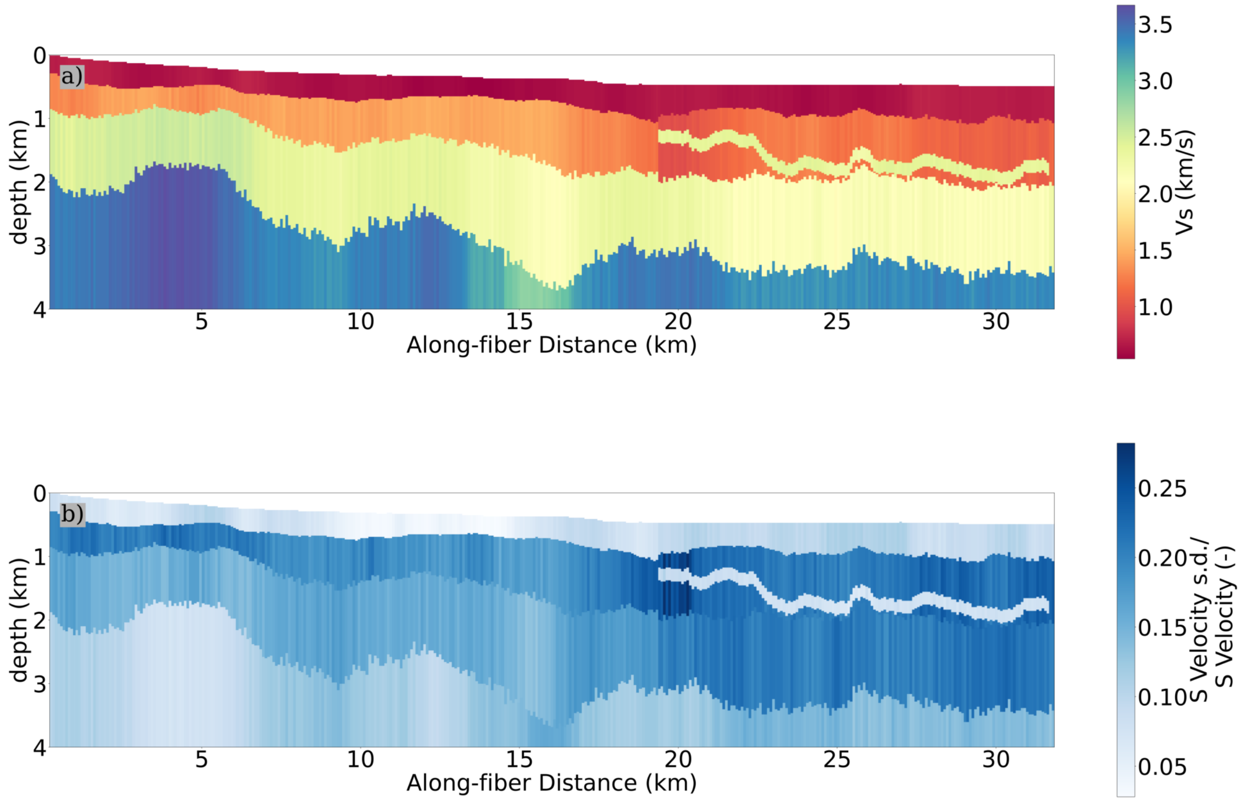

Figure 4 a) Along-fiber velocity model and b) velocity uncertainties. 2x vertical exaggeration. Layer thickness uncertainties are plotted in Figure S9

fit to the data, with observations of dispersion curves, delays between phases, and phase-amplitude ratios predicted within uncertainty (Figures 3, S4). The fit to data is approximately identical for a block of 0 m (Figure 3e-f) and 200 m (Figure 3c-d) thickness. In the former case, we assume that there is a layer in the subsurface producing a converted phase, but take said layer to be infinitesimally thin, such that it has no influence on the modeled dispersion curves. While such a layer is not physically realistic, comparing the infinitesimal result with one wherein the block has a finite thickness allows us to determine at what thickness the block becomes seismically visible through our dispersion curve data.

The layer velocities are also reasonable given the geologic environment. The top three layers have velocities consistent with valley fill under increasing compaction and lithification, while the bottom layer is consistent with an crystalline bedrock (Brocher, 2005). Our data cannot be fit with fewer than four layers and models quickly become unstable with more than four layers. However, a four-layer parameterization certainly cannot represent the full complexity of earth structure. The model imposes sharp jumps in velocity between adjacent layers of valley fill, which should not be interpreted as real features in the earth. Likewise, we observe a sharp reduction in the thickness of the first layer as we reach the location of the slumped block, and see fluctuations in the thickness of the third layer on high spatial frequencies, both of which are interpreted as artifacts of our model parameterization. We also perform an inversion with a parameterization that holds Vp and ρ constant, which yields similar results (Text S1, Figures S7-8).

Certain model parameters have high uncertainty, particularly the thicknesses and velocities of the second and third model layers along much of the array. These model parameters are expressed in the data through fine-scale changes in the slopes of the dispersion curves (whereas the velocities of the top and bottom layers are tied to the asymptotic behavior of the curves). Thus, any uncertainty in our dispersion curve observation leads to significant uncertainty in the behavior of the intermediate model layers.

While we smooth our data at several steps throughout the inversion, this smoothing is generally on a much shorter lengthscale than the features resolved by our model. We generally spatially average on a lengthscale of 500 m, while the layer thicknesses and velocities tend to vary on lengthscales of kilometers. While we perform a more intense spatial averaging in our initial, sparse inversion, the spatial averaging should not meaningfully bias our final, dense inversion.

4 Discussion

As the array crosses onto the proposed location of the NBB, the inversion indicates the top of the slumped block is located 730 ± 270 meters beneath the ground surface. The lower bound on this depth slightly exceeds the depth proposed for the block on the basis of resistivity data (400 m), but may agree within the error of the resistivity inversion (Hollett et al., 1989). As the array moves to the south, off of the proposed location, delays between the *P* and *Ps* arrivals increase, and in turn the modeled depth of the converting boundary increases to 1240 ± 340 m. Given that a southern portion of the block was not accounted for in past gravity-based inversions for the broader subsurface structure, such studies may have underestimated the depth to igneous bedrock beneath sedimentary valley fill in Owens Valley under Bishop, CA (as a layer of igneous rock may take on higher densities than the surrounding valley fill) (Saltus and Jachens, 1995). These new insights into the subsurface require further consideration, and may affect subsurface hydrological maps of Owens Valley (as the igneous base of the valley and the overlying sediment will likely differ in their porosity and permeability), a critical product in water resource management. We would expect that gravity-based studies could miss this unmapped portion of the NBB. At its unmapped locations, the NBB extends to increased depths, where it is likely bounded by higher density material. As the block was initially identified due to a density contrast with its surroundings, this could make observation through gravity data more challenging (Bateman et al., 1965; Hollett et al., 1989).

The uncertainty of the NBB velocity in our model is lower than that of surrounding layers. While surrounding layers are primarily constrained by dispersion curve data, the NBB velocity sees significant constraints from the *P*-*Ps* amplitude ratio (as demonstrated in Figure S10). Conversely, any uncertainty in the observation or forward-modeling of the *P*-*Ps* amplitude ratio should almost exclusively carry over to uncertainty in the NBB velocity.

We may compare our results with the interpretations of seismic refraction and gravity data reported in Pakiser and Kane (1962), though our fiber is displaced from all lines described in that study by at least several kilometers. As in that study, we infer that the sediment-bedrock interface dips to the west. We also observe a maximum depth for the interface of around three kilometers, which approximately agrees with gravity data. The seismic data in Pakiser and Kane (1962) suggests a shallower interface, on the order of one to two kilometers. One could reconcile these results by claiming that the deepest layer imaged in the study was in fact the NBB, and given that the authors were solely interpreting travel-time data, distinguishing a thinner, high velocity layer from the true bedrock interface would likely be challenging. Indeed, the depth of the bedrock observed through seismic refraction is more consistent with the depth of the NBB in our model. As the seismic survey in Pakiser and Kane (1962) is located several kilometers to the south of our fiber, one could also explain the observed disagreement by claiming the basin shallows to its south.

Note that our data do not conclusively indicate phase conversion by a slumped block, as our model could be consistent with a variety of geologic features with anomalously high velocity at depth. However, the feature we image is consistent in depth and location with that reported based on gravity and resistivity data, so we maintain an interpretation consistent with that past work (Hollett et al., 1989). Further, while a variety of features could produce the same data in practice, such alternative features have not been identified in the literature. Note that while volcanic ejecta from the Long Valley caldera, known as the Bishop Tuff, would likely take on similarly high wave speeds, well logs indicate that the tuff is significantly shallower than our observed anomaly in the region (Bateman et al., 1965).

Speaking more broadly, this study highlights the power of converted phases observed on fiber-optic arrays in densely imaging subsurface structure. While fiber-sensing cannot provide absolute amplitude or three-component information, as is typical of broadband seismic data, converted phases may arrive coherently on a dense array, and are thus often readily apparent in fiber-optic datasets. Such phases can impart valuable constraints on subsurface structure. Here, we can image an interface in the subsurface which could not be resolved as a sharp feature through traveltime or surface wave tomography. Further, the relative amplitude of direct and converted phases allows for a tightened constraint on velocities within the layer.

Future work reliant on converted phases observed through fiber-optic seismology will require a more mature approach to phase-picking (Atterholt and Zhan, 2024). The simple STA/LTA-based approach employed in this study is not viable for cases where the phase on any given channel may be below noise, and can only be identified through coherence across channels. Likewise, for a geologic setting wherein phases convert from dipping features, this approach would require more careful consideration of the change in the timing of converted phases with variations in backazimuth.

5 Conclusion

We have reinterpreted the subsurface structure in northern Owens Valley on the basis of data from a fiber-optic seismic array. Our interpretation is based on the joint inversion of ambient noise cross-correlations and converted phases. Our results indicate the continued presence of the North Bishop Block at increased depth to the south of its mapped extent, with relevance to subsurface hydrology. Broadly, our results highlight the underutilized power of converted phases observed on fiber-optic arrays in constraining sharp boundaries in subsurface structure. To more fully exploit the wealth of new fiber-optic seismic data in structural studies, our field must build up frameworks that better account for converted phases.

Acknowledgements

We appreciate valuable insights from Paul Asimow, Jean-Philippe Avouac, Drew Coleman, Jiaqi Fang, Jiaxuan Li, Auden Reid-McLaughlin, Joann Stock, Weiqiang Zhu, two anonymous reviewers, and handling editoars Suzan van der Lee and Joseph Byrnes.

Funding: This work was supported by the National Science Foundation (NSF) Faculty Early Career Development Program (CAREER), award number 1848166, and the Gordon and Betty Moore Foundation.

Data and code availability

Data and code are available through CaltechDATA (Bird, 2024). We provide virtual sources for each modeled channel, event data for each earthquake considered, and event picks from PhaseNet-DAS. The provided code allows users to replicate the inversion and plot all paper figures.

Competing interests

The authors declare that they have no competing interests.

References

Aki, K. and Richards, P. G. *Quantitative Seismology*. 2002.

Atterholt, J. and Zhan, Z. Fine-Scale Southern California Moho Structure Uncovered with Distributed Acoustic Sensing. *Science Advances*, 10(48):eadr3327, Nov. 2024. doi: 10.1126/sciadv.adr3327.

Bateman, P. C., Pakiser, L. C., and Kane, M. F. Geology and Tungsten Mineralization of the Bishop District, California, with a Section on Gravity Study of Owens Valley and a Section on Seismic Profile. Technical report, US Govt. Print. Off.„ 1965.

Biondi, E., Zhu, W., Li, J., Williams, E. F., and Zhan, Z. An Upper-Crust Lid over the Long Valley Magma Chamber. *Science Advances*, 9(42):eadi9878, Oct. 2023. doi: 10.1126/sciadv.adi9878.

Bird, E. Data and Code from 'Imaging the North Bishop Block with Converted Phases Observed through Fiber-Optic Seismology' Version 2 [dataset], 2024. doi: 10.22002/vxjcp-33r98.

Bird, E., Atterholt, J., Li, J., Biondi, E., Zhai, Q., Li, L., Yang, Y., Fang, J., Wei, X., Hjörleifsdóttir, V., Klesh, A., Kamalov, V., Gunnarsson, T., and Zhan, Z. Constraining Dike Opening Models With Seismic Velocity Changes Associated With the 2023–2024 Eruption Sequence on the Reykjanes Peninsula. *AGU Advances*, 6(1): e2024AV001516, 2025. doi: 10.1029/2024AV001516.

Brocher, T. M. Empirical Relations between Elastic Wavespeeds and Density in the Earth's Crust. *Bulletin of the Seismological Society of America*, 95(6):2081–2092, Dec. 2005. doi: 10.1785/0120050077.

Danskin, W. R. Evaluation of the Hydrologic System and Selected Water-Management Alternatives in the Owens Valley, California. Technical report, 1998. doi: 10.3133/wsp2370H.

Dou, S., Lindsey, N., Wagner, A. M., Daley, T. M., Freifeld, B., Robertson, M., Peterson, J., Ulrich, C., Martin, E. R., and Ajo-Franklin, J. B. Distributed Acoustic Sensing for Seismic Monitoring of The Near Surface: A Traffic-Noise Interferometry Case Study. *Scientific Reports*, 7(1):11620, Sept. 2017. doi: 10.1038/s41598-017-11986-4.

Fang, J., Yang, Y., Shen, Z., Biondi, E., Wang, X., Williams, E. F., Becker, M. W., Eslamian, D., and Zhan, Z. Directional Sensitivity of DAS and Its Effect on Rayleigh-Wave Tomography: A Case Study in Oxnard, California. *Seismological Research Letters*, 94 (2A):887–897, Nov. 2022. doi: 10.1785/0220220235.

Foreman-Mackey, D., Hogg, D. W., Lang, D., and Goodman, J. Emcee: The MCMC Hammer. https://arxiv.org/abs/1202.3665v4, Feb. 2012. doi: 10.1086/670067.

Herrmann, R. B. Computer Programs in Seismology: An Evolving Tool for Instruction and Research. *Seismological Research Letters*, 84(6):1081–1088, Nov. 2013. doi: 10.1785/0220110096.

Hollett, K. J., Danskin, W. R., McCaffrey, W. F., and Walti, C. L. Geology and Water Resources of Owens Valley, California. Technical report, US Geological Survey, 1989.

Klaasen, S., Thrastarson, S., Çubuk-Sabuncu, Y., Jónsdóttir, K., Gebraad, L., Paitz, P., and Fichtner, A. Subglacial Volcano Monitoring with Fibre-Optic Sensing: Grímsvötn, Iceland. *Volcanica*, 6 (2):301–311, Sept. 2023. doi: 10.30909/vol.06.02.301311.

Langston, C. A. Structure under Mount Rainier, Washington, Inferred from Teleseismic Body Waves. *Journal of Geophysical Research: Solid Earth*, 84(B9):4749–4762, 1979. doi: 10.1029/JB084iB09p04749.

LAWDP. Facts & History - Los Angeles Department of Water and Power. https://www.ladwp.com/who-we-are/water-system/los-angeles-aqueduct/facts-history, 2024.

Leahy, G. M., Saltzer, R. L., and Schmedes, J. Imaging the Shallow Crust with Teleseismic Receiver Functions. *Geophysical Journal International*, 191(2):627–636, Nov. 2012. doi: 10.1111/j.1365-246X.2012.05615.x.

Li, J., Zhu, W., Biondi, E., and Zhan, Z. Earthquake Focal Mechanisms with Distributed Acoustic Sensing. *Nature Communications*, 14(1):4181, July 2023. doi: 10.1038/s41467-023-39639-3.

Pakiser, L. C. and Kane, M. F. Geophysical Study of Cenozoic Geologic Structures of Northern Owens Valley, California. *Geophysics*, 27(3):334–342, June 1962. doi: 10.1190/1.1439021.

Roth, N., Zhu, T., Czarny, R., and Gao, Y. Wavefield Modeling and Analysis of Lightning Quakes Measured by a Distributed Acoustic Sensing Array. *Bulletin of the Seismological Society of America*, Oct. 2023. doi: 10.1785/0120230116.

Saltus, R. W. and Jachens, R. C. Gravity and Basin-Depth Maps of the Basin and Range Province, Western United States. Technical report, 1995.

Shen, J. and Zhu, T. DAS with Telecommunication Fibre-Optic Cable in Urban Areas Can Record Storm-Induced Seismic Noise. *Geophysical Journal International*, 235(3):2122–2136, Dec. 2023. doi: 10.1093/gji/ggad352.

Song, Z., Zeng, X., Chi, B., Bao, F., and Osotuyi, A. G. Using the Three-Station Interferometry Method to Improve Urban DAS Ambient Noise Tomography. *Frontiers in Earth Science*, 10, 2022. doi: 10.3389/feart.2022.952410.

Stevens, C. H., Stone, P., and Blakely, R. J. Structural Evolution of the East Sierra Valley System (Owens Valley and Vicinity), California: A Geologic and Geophysical Synthesis. *Geosciences*, 3 (2):176–215, 2013. doi: 10.3390/geosciences3020176.

Tsai, V. C. The Future of Earth Imaging. *Seismological Research Letters*, 94(5):2119–2128, Aug. 2023. doi: 10.1785/0220230125.

Wang, X., Williams, E. F., Karrenbach, M., Herráez, M. G., Martins, H. F., and Zhan, Z. Rose Parade Seismology: Signatures of Floats and Bands on Optical Fiber. *Seismological Research Letters*, 91 (4):2395–2398, May 2020. doi: 10.1785/0220200091.

Williams, E. F., Fernández-Ruiz, M. R., Magalhaes, R., Vanthillo, R., Zhan, Z., González-Herráez, M., and Martins, H. F. Distributed Sensing of Microseisms and Teleseisms with Submarine Dark Fibers. *Nature Communications*, 10(1):5778, Dec. 2019. doi: 10.1038/s41467-019-13262-7.

Yang, Y., Atterholt, J. W., Shen, Z., Muir, J. B., Williams, E. F., and Zhan, Z. Sub-Kilometer Correlation Between Near-Surface Structure and Ground Motion Measured With Distributed Acoustic Sensing. *Geophysical Research Letters*, 49(1): e2021GL096503, 2022. doi: 10.1029/2021GL096503.

Yin, J., Zhu, W., Li, J., Biondi, E., Miao, Y., Spica, Z. J., Viens, L., Shinohara, M., Ide, S., Mochizuki, K., Husker, A. L., and Zhan, Z. Earthquake Magnitude With DAS: A Transferable Data-Based Scaling Relation. *Geophysical Research Letters*, 50(10): e2023GL103045, 2023. doi: 10.1029/2023GL103045.

Yu, C., Zhan, Z., Lindsey, N. J., Ajo-Franklin, J. B., and Robertson, M. The Potential of DAS in Teleseismic Studies: Insights From the Goldstone Experiment. *Geophysical Research Letters*, 46(3): 1320–1328, 2019. doi: 10.1029/2018GL081195.

Zhan, Z. Distributed Acoustic Sensing Turns Fiber-Optic Cables into Sensitive Seismic Antennas. *Seismological Research Letters*, 91(1):1–15, 2020. doi: 10.1785/0220190112.

Zhu, W., Biondi, E., Li, J., Yin, J., Ross, Z. E., and Zhan, Z. Seismic Arrival-Time Picking on Distributed Acoustic Sensing Data Using Semi-Supervised Learning. *Nature Communications*, 14(1): 8192, Dec. 2023. doi: 10.1038/s41467-023-43355-3.